ACS OMEGA

http://pubs.acs.org/journal/acsodf

Article

Surface Modification of ZnO Nanocrystals with Conjugated Polyelectrolytes Carrying Different Counterions for Inverted Perovskite Light-Emitting Diodes

Fu-Bing Chiu, You-Wei Wu, and Sheng-Hsiung Yang*

Cite This: *ACS Omega* 2023, 8, 19109−19118

Read Online

ACCESS | Metrics & More | Article Recommendations | Supporting Information

ABSTRACT: In this work, bromide ions (Br^-) on the conjugated polyelectrolytes (CPEs) were converted to tetrafluoroborate (BF_4^-) or hexafluorophosphate (PF_6^-) ions through anion exchange. The three CPEs (PFN-Br, PFN-BF_4, and PFN-PF_6) were utilized solely for surface modification of zinc oxide nanocrystals (ZnO NCs). The ionic groups on CPEs can form permanent dipoles to facilitate charge injection from ZnO NCs to cesium lead bromide ($CsPbBr_3$) NC emitters, therefore promoting luminescent properties of inverted perovskite light-emitting diodes (PeLEDs). The experimental results reveal that ZnO NC films were smoothened by CPEs that allowed flat deposition of the perovskite active layers; moreover, the improved contact between ZnO and perovskite layers was beneficial for reducing leakage current, as verified in the dark current measurement of devices. In addition, the incorporation of CPEs helped to passivate the defects of ZnO NC films and prolong the carrier lifetime of $CsPbBr_3$ NCs. PeLEDs based on different CPEs were then constructed and evaluated. The device based on PFN-Br showed the highest brightness and current efficiency, and the one based on PFN-BF_4 exhibited better current efficiency over PFN-Br under the low current density below 160 mA/cm^2. This is the first report using fluorene-based CPEs with Br^-, BF_4^-, or PF_6^- groups to modify the properties of ZnO and $CsPbBr_3$ NCs for the construction of inverted PeLEDs so far. Our experiments explored new kinds of CPEs on the surface modification of ZnO NCs and device performance of PeLEDs.

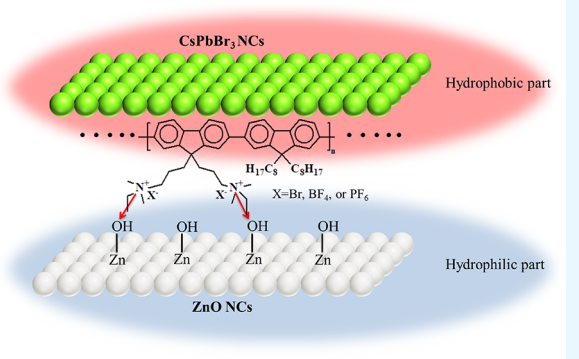

INTRODUCTION

In recent years, hybrid organic−inorganic perovskite materials have attracted significant attention because of their solution processability, superior color purity, tunable bandgap, high photoluminescence quantum yield (PLQY), and low cost.[1−5] They can be applied to the fields of perovskite solar cells, lasers, photodetectors, and perovskite light-emitting diodes (PeLEDs).[6−9] To improve the performance of perovskite materials, various dimensional nanostructures have been developed such as nanorods, nanowires, nanoplatelets, and nanocrystals (NCs).[10−13] Among the above four nanostructures, perovskite NCs are the best candidate for fabricating light-emitting devices because they can form compact and uniform thin layers by a solution process with minimized defects. In 2015, the first study concerning all-inorganic cesium lead halide ($CsPbX_3$, X = Cl, Br, and I) NCs was released,[14] which opened a new research direction toward highly stable and luminescent perovskite-related materials. The mainstream way to prepare all-inorganic perovskite NCs is the hot-injection method;[15] some other methods have also been reported, including ligand-assisted reprecipitation, microwave-assisted synthesis, ultrasonication, and solvothermal synthesis.[16−19] Oleic acid (OA) and oleylamine (OAm) are common surface ligands to control the stability of perovskite NCs, yet both of them possess insulating long carbon chains to hinder carrier transport. To solve this drawback, Pan et al. employed a relatively short ligand didodecyldimethylammonium bromide to replace partial long carbon chain ligands to improve the charge carrier balance, and the corresponding PeLED achieved a maximum brightness (L_{max}) and external quantum efficiency (EQE) of 330 cd/m^2 and 3.0%, respectively.[20] He et al. introduced phenethylammonium bromide (PEABr) to passivate the halide vacancies on $CsPbBr_3$ NCs, which are regarded as undesirable recombination sites to deplete carriers.[21] Also, the π-conjugated benzene ring contributes to the charge transport. The PeLED based on PEABr-passivated $CsPbBr_3$ NCs exhibited an EQE of 6.85% and a current efficiency of 23.79 cd A^{-1}.

Received: April 16, 2023
Accepted: May 9, 2023
Published: May 18, 2023

N-type zinc oxide (ZnO) often acts as the electron transport layer (ETL) in inverted PeLEDs because of its good electrical conductivity, high transparency in the visible region, good air stability, and facile solution processability.[22,23] A sol−gel method is extensively applied to prepare ZnO NC films at room temperature, using sodium hydroxide or tetramethylammonium hydroxide to conduct hydrolysis.[24,25] Although ZnO NCs can facilitate the performance of inverted PeLEDs, the surface traps and defects of NCs usually lead to exciton quenching that requires surface passivation to augment device performance.[26] In addition, the electron mobility of ZnO is higher than commonly used hole-transporting small molecules, such as 4,4′,4″-tris(4-carbazoyl-9-ylphenyl)amine (TCTA),[27] leading to carrier imbalance and low device performance. As a result, selecting suitable interfacial modification layers to insert between the ETL and the perovskite active layer is extremely important. Kumar et al. deposited a transparent and insulating poly(methylmethacrylate) (PMMA) film between ZnO and the perovskite emitter to inhibit nonradiative recombination and reduce leakage current in devices.[28] The performance of the device containing a PMMA interlayer was six-fold higher compared with the controlled device without PMMA. Huang and coworkers adopted polyethyleneimine (PEI) to improve the surface coverage, PL lifetime, and crystalline properties of perovskite films.[29] The optimized PeLED exhibited an EQE of 3.5% at 2.2 V, corresponding to an internal quantum efficiency of 15.7% and a radiance of 28 W sr^{-1} m^{-2}. Apart from PMMA and PEI, a conjugated polyelectrolyte (CPE), namely, poly[(9,9-bis(3′-(*N*,*N*-dimethyl)-*N*-ethylammoinium)-propyl-2,7-fluorene)-*alt*-2,7-(9,9-dioctylfluorene)]dibromide (PFN-Br), also serves as a surface modifier to modify the surface of ZnO.[30] The PFN-Br-modified ZnO has a lower roughness due to its positive pendant N^+ groups adsorbed toward the hydrophilic surface of ZnO films preferentially. Moreover, the existence of PFN-Br can convert the surface of ZnO films from hydrophilic to hydrophobic, which is beneficial for the deposition of the up-lying perovskite layer.

As mentioned in the previous paragraph, PFN-Br is a potential surface modifier that has been applied for fabricating blue PeLEDs.[31] After surveying the literature, we realize that PFN-Br is generally utilized in perovskite solar cells, while its application in the field of PeLEDs is much less reported. Moreover, it is necessary to develop new materials to expand the diversity of research instead of adopting limited materials for device fabrication. In addition to PFN-Br, the counterions on the ammonium groups can be interchanged from bromide ions (Br^-) to tetrafluoroborate (BF_4^-) or hexafluorophosphate (PF_6^-) ions through anion exchange to give two corresponding CPEs PFN-BF_4 or PFN-PF_6, respectively. In this study, we carried out a facile synthesis to covert Br^- to BF_4^- or PF_6^- groups with moderate yields. The obtained CPEs were then utilized to modify surface properties of ZnO NCs. The schematic illustration of the interaction between the CPEs and ZnO NCs is depicted in Figure 1. To the best of our knowledge, the above two CPEs have not been utilized in perovskite NC-related research. This is the first time that the fluorene-based CPEs containing Br^-, BF_4^-, or PF_6^- groups are utilized to modify the properties of ZnO and $CsPbBr_3$ NCs for fabricating inverted PeLEDs. We expect that more effective charge injection into the perovskite layer can be achieved through those fluorine-rich groups to enhance device performance. Inverted PeLEDs with the configuration of ITO/ZnO NCs/PFN-Br or PFN-BF_4 or PFN-PF_6)/$CsPbBr_3$ NCs/TCTA/molybdenum(VI) oxide (MoO_3)/Au were fabricated and evaluated. The influence of different CPEs on the properties of low-lying ZnO and up-lying $CsPbBr_3$ NCs was also explored.

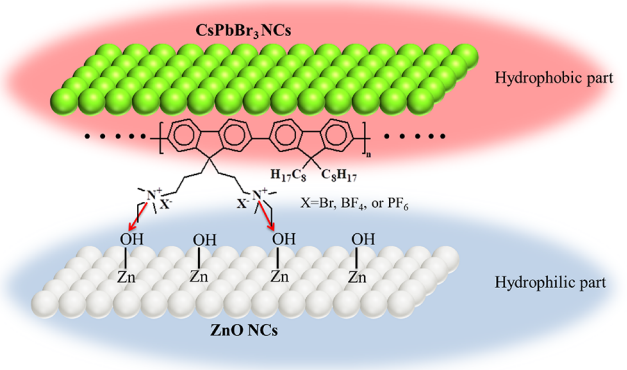

Figure 1. Schematic illustration of the interaction between the CPEs and ZnO NCs.

EXPERIMENTAL SECTION

Materials. Indium tin oxide (ITO) glass substrates (15 Ω/square) were purchased from Aimcore Technology. Cesium carbonate (Cs_2CO_3, 99.995%), octadec-1-ene (ODE, 90%), and OAm (80−90%) were received from Acros. Lead bromide ($PbBr_2$, 99.998%), zinc acetate dihydrate ($Zn(CH_3COO)_2 \cdot 2H_2O$, 98%), sodium tetrafluoroborate ($NaBF_4$, 97%), and MoO_3 (99.95%) were bought form Alfa Aesar. OA (90%), ammonium hexafluorophosphate (NH_4PF_6, 99%), and PFN-Br were bought from Sigma-Aldrich. Sodium beta-styrenesulfonate (S*β*SS) and TCTA (99.5%) were purchased from TCI and Lumtec, respectively. Other chemicals and solvents were received from Alfa Aesar, Acros, or TEDIA and used without further purification. In addition, ZnO NC dispersions were prepared according to the previous study.[32]

Preparation of PFN-BF_4 and PFN-PF_6. To prepare PFN-BF_4, 50 mg of PFN-Br and 131 mg (1.2 mmol) of $NaBF_4$ were added to 20 mL of methanol and stirred for 2 days at room temperature. The reaction mixture was then condensed by rotary evaporation to remove the solvent. The above procedure was repeated for 5 times to attain a high percentage of ionic exchange from Br^- to BF_4^-. Afterward, 100 mL of deionized (DI) water was poured into the mixture and stirred for 8 h. The precipitate was collected and dried in an oven at 100 °C to give the final product PFN-BF_4 as a yellow solid (38.6 mg, 76%). As for PFN-PF_6, 50 mg of PFN-Br, 195 mg (1.2 mmol) of NH_4PF_6, and 20 mL of methanol were used. The synthetic procedure was similar to that of PFN-BF_4, giving the final product PFN-PF_6 as a pale yellow solid (44.2 mg, 77%).

Synthesis of $CsPbBr_3$ NCs. Cs_2CO_3 (407 mg, 1.25 mmol), 1.25 mL of OA, and 20 mL of ODE were added to a 100 mL two-neck flask, and the mixture was heated at 120 °C under vacuum for 1 h. Afterward, the mixture was heated to 160 °C for 30 min under nitrogen until all solid was dissolved to give Cs-oleate.

$PbBr_2$ (138 mg, 0.376 mmol), 20 mg (0.097 mmol) of S*β*SS, 0.6 mL of OA, 1 mL of OAm, and 10 mL of ODE were added to a 100 mL two-neck flask. The mixture was heated to 120 °C for 1 h followed by raising the temperature to 160 °C for 20 min under nitrogen to obtain Pb-oleate. After that, 0.8 mL of

https://doi.org/10.1021/acsomega.3c02593
ACS Omega 2023, 8, 19109−19118

Cs-oleate was quickly injected into the Pb-oleate solution using a syringe. After 5 s, the reaction flask was immersed in an ice bath immediately. The crude product was centrifuged at 8500 rpm for 5 min, the supernatant was discarded, and the precipitate was dispersed in 2 mL of *n*-hexane. After adding 8 mL of ethyl acetate, the solution was centrifuged again at 8500 rpm for 5 min, and the precipitate was redispersed in 2 mL of *n*-hexane for further use.

Device Fabrication. The ITO substrates were cleaned sequentially with detergent, DI water, acetone, and isopropyl alcohol (IPA) and purged with nitrogen flow followed by oxygen plasma treatment for 3 min. The ZnO NC dispersion was spin-coated onto the ITO substrate at 3000 rpm for 30 s and annealed at 150 °C for 20 min. PFN-Br (0.5 mg/mL in methanol), PFN-BF_4 (0.5 mg/mL in acetonitrile), or PFN-PF_6 (0.5 mg/mL in acetonitrile) was individually spin-coated onto the ZnO NC layer at 4000 rpm for 30 s and dried at 110 °C for 20 min. The concentration of the three CPEs (0.5 mg/mL) was referred to the literature,[30,31] all stating that 0.5 mg/mL was the optimal parameter for the preparation of CPE solutions. The $CsPbBr_3$ NCs solution was then spin-coated onto the PFN-Br (or PFN-BF_4, PFN-PF_6) layer at 4000 rpm for 60 s and heated at 80 °C for 20 min. Afterward, TCTA, MoO_3, and Au electrodes were sequentially deposited by thermal evaporation. The active area of each device was 1 mm^2.

Characterization Methods. The identification of anion exchange from PFN-Br to PFN-BF_4 or PFN-PF_6 was carried out with a Thermo K-Alpha X-ray photoelectron spectrometer (XPS). The crystalline structure and size of $CsPbBr_3$ NCs were investigated by a JEOL JEM-3010 transmission electron microscope (TEM). The top-view and cross-sectional scanning electron microscopy (SEM) micrographs of ZnO NCs and perovskite films were obtained by an ultrahigh-resolution ZEISS crossbeam SEM. The surface morphology and average roughness (R_a) of samples were verified with a Bruker Innova atomic force microscope (AFM) with a tapping mode. The diffraction patterns of perovskite films on different modification layers were conducted by a Bruker D8 SSS X-ray diffractometer (XRD). The wavelength of the light source was 1.54 Å. The absorption and photoluminescence (PL) spectra were recorded with a Princeton Instruments Acton 2150 spectrophotometer equipped with a xenon lamp (ABET Technologies LS 150) as the light source. The electroluminescence (EL) spectra and device performance of light-emitting devices were acquired by an Agilent 4155C semiconductor parameter analyzer and an Ocean Optics USB2000+ spectrometer. The time-resolved photoluminescence (TR-PL) decay signals were recorded by a time-related single-photon counting module (PicoQuant MultiHarp 150 4N) combined with a photomultiplier tube through an Andor Kymera 328i spectrometer with the time resolution of 160 ps. A 473 nm pulsed laser (Omicron) was used as an excitation source with a beam time width of 90 ps.

RESULTS AND DISCUSSION

Figure 2 shows the chemical structures of the three CPEs (PFN-Br, PFN-BF_4, and PFN-PF_6) utilized to modify the surface properties of ZnO NCs in this study. Figure S1 displays the XPS spectra of PFN-Br, PFN-BF_4, and PFN-PF_6 before and after anion exchange. In Figure S1a in the Supporting Information, a clear Br 3d signal was located at around 66−69 eV for PFN-Br; after anion exchange, this Br 3d peak

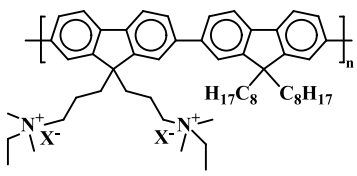

PFN-Br, X = Br
PFN-BF_4, X = BF_4
PFN-PF_6, X = PF_6

Figure 2. Chemical structures of PFN-Br, PFN-BF_4, and PFN-PF_6.

disappeared for PFN-BF_4 and PFN-PF_6.[33] Meanwhile, the B 1s and P 2p peaks at 193.2 and 135.5 eV were observed for PFN-BF_4 and PFN-PF_6, respectively, as revealed in Figure S1b,c.[34,35] In addition, the F 1s peak was detected at 685.1 and 685.8 eV for both PFN-BF_4 and PFN-PF_6, respectively, as shown in Figure S1d.[36] The slight energy difference of the F 1s signal between PFN-BF_4 and PFN-PF_6 can be attributed to different chemical environments of the F element on the BF_4 and PF_6 groups. The central P atom of the PF_6 group is more electronegative than the B atom of the BF_4 group (electronegativity 2.19 vs 2.04). The slightly decreased shielding brought by the P atom increases the effective attractive force of the F nucleus with regard to its 1s core electrons, shifting the XPS peak to higher binding energies. Therefore, PFN-BF_4 and PFN-PF_6 were successfully obtained from PFN-Br through anion exchange. To investigate the effect of different CPEs on the surface morphology and roughness of ZnO NC films, SEM and AFM experiments were performed. The top-view SEM images of the original and CPE-modified ZnO NC films are provided in Figure S2 in the Supporting Information. All samples showed homogeneous and dense distribution of NCs. The topographic AFM images of ZnO NC films before and after depositing PFN-Br, PFN-BF_4, or PFN-PF_6 are provided in Figure S3. The original ZnO NC film had an R_a value of 1.58 nm; after depositing PFN-Br, PFN-BF_4, or PFN-PF_6, the R_a values of the modified films were reduced to 0.81, 1.19, and 1.38 nm, respectively, indicating that CPEs can effectively smoothen the surface of ZnO NC films. Among them, coarse particles were observed on the PFN-PF_6-modified ZnO NC film, which may be due to agglomeration of the CPE carrying PF_6 groups.

To analyze the interaction between ZnO and CPEs, XPS measurements were performed, and related results of the original ZnO NCs as well as PFN-Br-, PFN-BF_4-, and PFN-PF_6-modified ZnO NCs are depicted in Figure S4. Figure S4a shows the O 1s core-level signal of the original ZnO NCs fitted by three Gaussian components at 529.6, 531.1, and 532.0 eV that correspond to the O−Zn bond in the lattice, O−H hydroxyl group, and adsorbed H_2O, respectively.[37] After depositing PFN-Br, PFN-BF_4, or PFN-PF_6, the component of the O−Zn bond was basically unchanged, as displayed in Figure S4b−d. Furthermore, the O−H components were shifted to 531.4, 531.1, and 531.2 eV, respectively. The larger peak shift from PFN-Br-modified ZnO suggests a stronger interaction between the $-R_3N^+Br^-$ group and the O−H group on ZnO compared to the other two CPEs. Other elemental signals like Br 3d, B 1s, P 2p, and F 1s are provided in Figure S5 to further verify the existence of CPEs.

The energy levels of the original and CPE-modified ZnO NC films were calculated from their UPS spectra in Figure 3. The work function (φ_w) is defined as the energy difference between the Fermi level (E_F) and the vacuum level (0 eV),

https://doi.org/10.1021/acsomega.3c02593
ACS Omega 2023, 8, 19109−19118

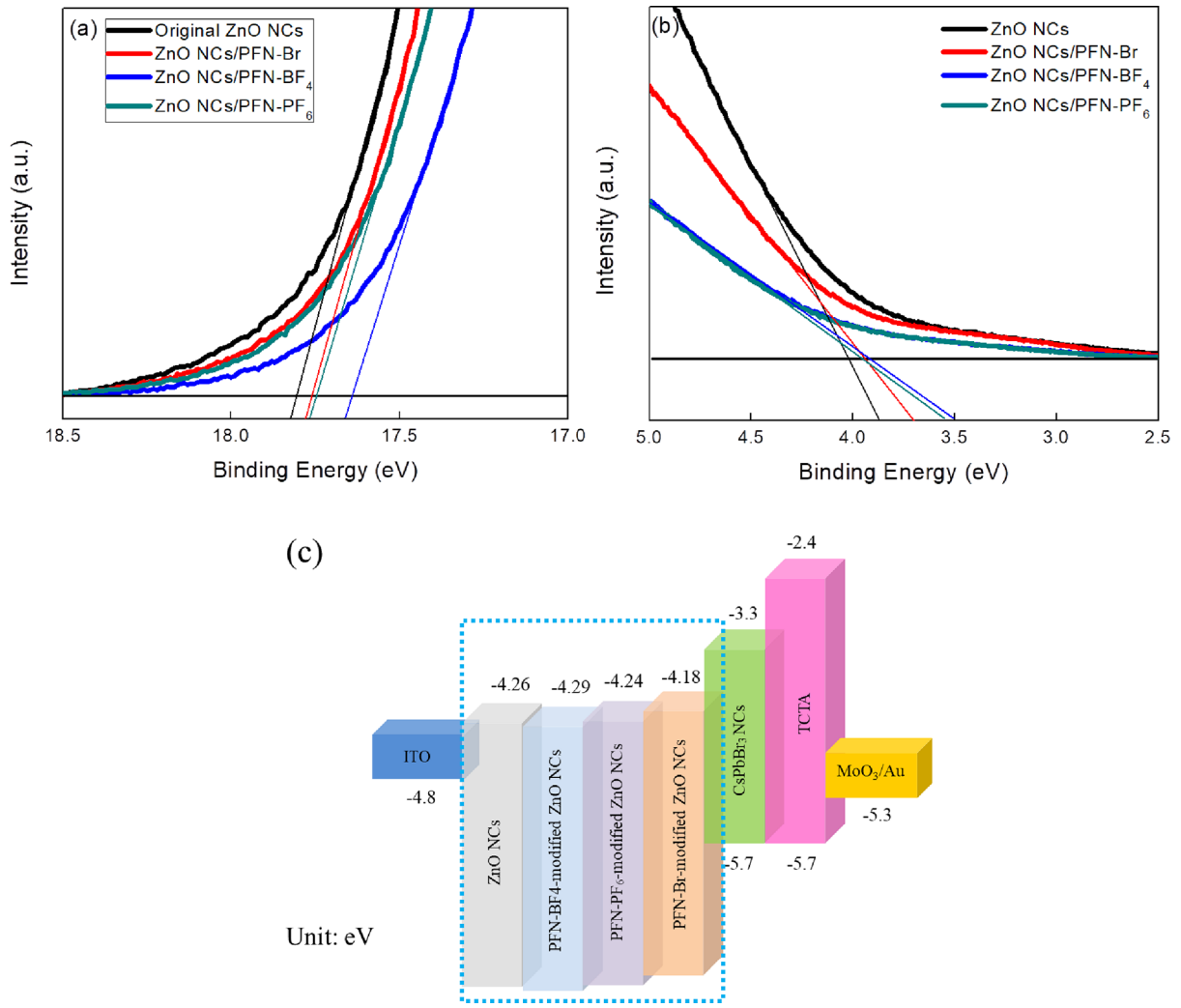

Figure 3. UPS spectra of the original and CPE-modified ZnO NCs at (a) high- and (b) low-binding-energy regions; (c) energy level diagram of the whole PeLED.

which is affirmed by subtracting the cutoff in the high-binding-energy region (about 17.7 eV) from the He I photon energy (21.22 eV), wherefore the E_F of the original ZnO NC film was calculated to be −3.46 eV. The E_F values of the other three ZnO NC films modified by PFN-Br, PFN-BF_4, and PFN-PF_6 were calculated to be −3.48, −3.59, and −3.50 eV, respectively. The low-binding-energy cutoff (around 4.0 eV) is relevant to the energy difference between the valence band (VB) and the E_F; therefore, the VB values of the ZnO NC films without and with PFN-Br, PFN-BF_4, and PFN-PF_6 modification were calculated to be −7.49, −7.41, −7.52, and −7.47 eV, respectively. The obtained VB values of ZnO NC films in this study are close to the reported values in the literature.[38,39] To lead out the conduction band (CB), the energy bandgap (E_g) of ZnO NCs without and with CPEs should be acquired first. Figure S6a shows the absorption spectra of the original and CPE-modified ZnO NC films, and the E_g of ZnO NCs is estimated from the Tauc plot in Figure S6b to be 3.23 eV. It is noted that the additional absorption band at 390 nm for CPE-modified ZnO NCs is originated from the deposited PFN-Br, PFN-BF_4, and PFN-PF_6, which own conjugated main chains. Hence, the CB values of the original ZnO NC film and PFN-Br-, PFN-BF_4-, and PFN-PF_6-modified ZnO NC films are derived to be −4.26, −4.18, −4.29, and −4.24 eV, respectively. The energy levels of ZnO NCs before and after CPE modification are then established in Figure 3c. It is clearly seen that the upshifted CB of ZnO NCs modified by PFN-Br demonstrates the most advantageous charge injection among the three CPEs in Figure 3c, owing to the reduced energy barrier between the ZnO ETL and the $CsPbBr_3$ active layer.

To identify the crystalline morphology and size of $CsPbBr_3$ NCs via the hot-injection method, TEM and HR-TEM experiments were executed. Figure S7a presents homogeneous cubic crystallites of $CsPbBr_3$ NCs and the lattice spacing of 0.58 nm, which is consistent with the (100) plane of the cubic lattice structure.[40] The average crystalline size of $CsPbBr_3$ NCs is calculated to be 11.58 nm from their size distribution histogram in Figure S7b. To comprehend the influence of different CPEs on the deposition of $CsPbBr_3$ NCs on ZnO NC films, SEM and AFM examinations were implemented. The top-view SEM and topographic AFM images of $CsPbBr_3$ NCs on the original and CPE-modified ZnO NC films are displayed in Figures 4 and 5, respectively. In Figure 4, it is seen that densely packed $CsPbBr_3$ NCs can be deposited on the four ZnO NC films without pinholes, and less aggregation is observed on those ZnO after CPE modification. Turning to Figure 5, all samples show a nanoparticle-aggregated morphology. The R_a value of $CsPbBr_3$ NCs on the original

https://doi.org/10.1021/acsomega.3c02593
ACS Omega 2023, 8, 19109−19118

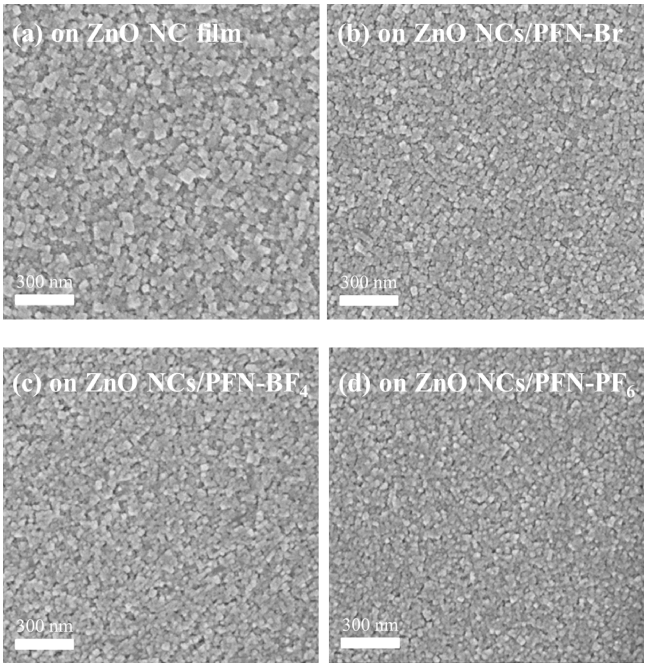

Figure 4. Top-view SEM images of $CsPbBr_3$ NCs on the (a) original and (b) PFN-Br-, (c) PFN-BF_4-, and (d) PFN-PF_6-modified ZnO NC films.

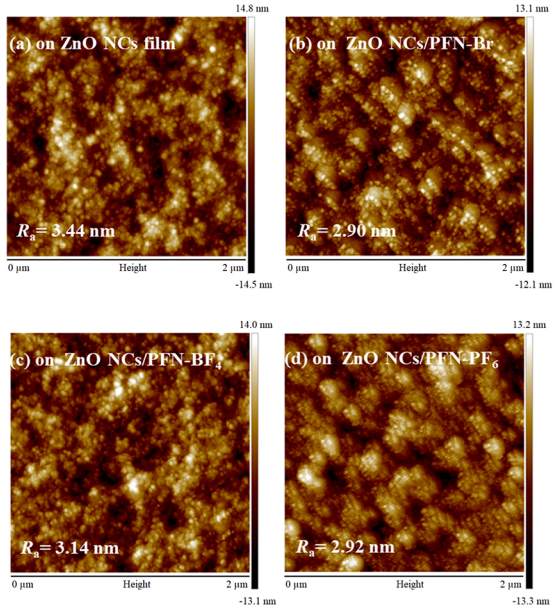

Figure 5. AFM topographic images of $CsPbBr_3$ NCs on the (a) original and (b) PFN-Br-, (c) PFN-BF_4-, and (d) PFN-PF_6-modified ZnO NC films.

ZnO was measured to be 3.44 nm, while it decreased to 2.90, 3.14, and 2.92 nm on PFN-Br-, PFN-BF_4-, and PFN-PF_6-modified ZnO. The reduced aggregation and surface roughness of $CsPbBr_3$ NCs on the CPE-modified ZnO NC films can be explained as follows. First, the incorporation of CPEs is proven to flatten the surface of ZnO NC films that is favorable for the deposition of smooth $CsPbBr_3$ NC layers, as mentioned in the previous part. Second, the ionic ammonium groups on CPEs tend to approach the hydrophilic ZnO, and thus, hydrophobic conjugated backbones locate on the upper surface, as displayed in Figure 1. Since $CsPbBr_3$ NCs are dispersed in a nonpolar solvent, i.e., *n*-hexane, better contact between the $CsPbBr_3$ dispersion and the CPE surface is achieved, and smoother perovskite NC films are obtained.[41]

The absorption spectra of $CsPbBr_3$ deposited on ZnO NC films without and with PFN-Br, PFN-BF_4, or PFN-PF_6 are provided in Figure 6a. The $CsPbBr_3$ NCs on the original ZnO NC film show an absorption maximum at 420 nm and an absorption edge at *ca.* 529 nm;[42] by inserting an ultrathin PFN-Br, PFN-BF_4, or PFN-PF_6 layer between the perovskite and ZnO NCs, the absorption maxima are slightly blueshifted to 410 nm, which can be ascribed to the absorption behavior of the CPEs on ZnO at around 390 nm, as shown in Figure S6a. The Tauc plot of $CsPbBr_3$ NCs is displayed in Figure S8, indicative of an optical bandgap of 2.4 eV. The bandgap of $CsPbBr_3$ NCs is not affected by different CPEs since it is determined after the hot-injection synthesis of NCs. The PL emission spectra of $CsPbBr_3$ on different ETLs are depicted in Figure 6b. All of them display a green emission at 510 nm and a narrow full-width at half-maximum (FWHM) of 28 nm. Compared to the original ZnO NCs, the $CsPbBr_3$ NCs deposited on the CPE-modified ZnO are found to have stronger PL emission. Moreover, the PLQY value of the $CsPbBr_3$ NC film was improved from 16% on the original ZnO NC film to 54, 42, and 33% on PFN-Br-, PFN-BF_4-, PFN-PF_6-modified ZnO NC films, respectively. It is reported that direct contact between $CsPbBr_3$ NCs and metallic oxide can lead to quenching of photogenerated carriers to attenuate PL emission.[26,43] The introduction of CPEs like PFN-Br, PFN-BF_4, and PFN-BF_6, can effectively passivate surface traps of ZnO to preserve PL emission of the upper $CsPbBr_3$ NCs, especially PFN-Br that has the highest PL intensity among all samples. To investigate the effect of CPE-modified ZnO NCs on the radiative recombination process of $CsPbBr_3$ NCs, the TR-PL decay measurement was implemented, and corresponding PL decay curves are depicted in Figure 6c, which were fitted by a biexponential decay function.[44,45] The detailed parameters for TR-PL decay measurements are listed in Table S1 in the Supporting Information. The average carrier lifetime (τ_{avg}) of $CsPbBr_3$ NCs on the original ZnO NC film was calculated to be 5.74 ns, while it increased to 13.71, 10.37, and 8.78 ns for those $CsPbBr_3$ NCs deposited on the PFN-Br-, PFN-BF_4-, and PFN-PF_6-modified ZnO, respectively. Herein, the CPE modification helped to passivate surface defects of ZnO and therefore to prolong the carrier lifetime of $CsPbBr_3$ NCs. In addition, the XRD patterns of $CsPbBr_3$ NCs on different ZnO NC films are demonstrated in Figure 6d. All samples exhibit similar characteristic peaks at 2θ = 15.14, 21.4, 30.44, and 37.60°, corresponding to the (100), (110), (200), and (211) planes, respectively, which are well-consistent with the cubic phase of $CsPbBr_3$.[46] No peak shift or additional peak was observed, meaning that the lattice structure of $CsPbBr_3$ is the same on the original and CPE-modified ZnO NC films. It is noted that $CsPbBr_3$ NCs on the PFN-PF_6-modified ZnO own the strongest peak intensity, implying that the highest degree of crystallinity was achieved when using PFN-PF_6.

The PeLED device with the configuration of ITO/CPE-modified ZnO NCs/$CsPbBr_3$ NCs/TCTA/MoO_3/Au is provided in Figure 7a. The cross-sectional SEM image of the PeLED is revealed in Figure 7b, indicating the layer thicknesses of 30, 30, 40, and 100 nm for the modified ZnO NCs, $CsPbBr_3$ NCs, TCTA, and MoO_3/Au, respectively. It is difficult to detect the real thickness of CPEs by SEM because their concentration in solutions is very low. Hence, the thickness of

https://doi.org/10.1021/acsomega.3c02593
ACS Omega 2023, 8, 19109−19118

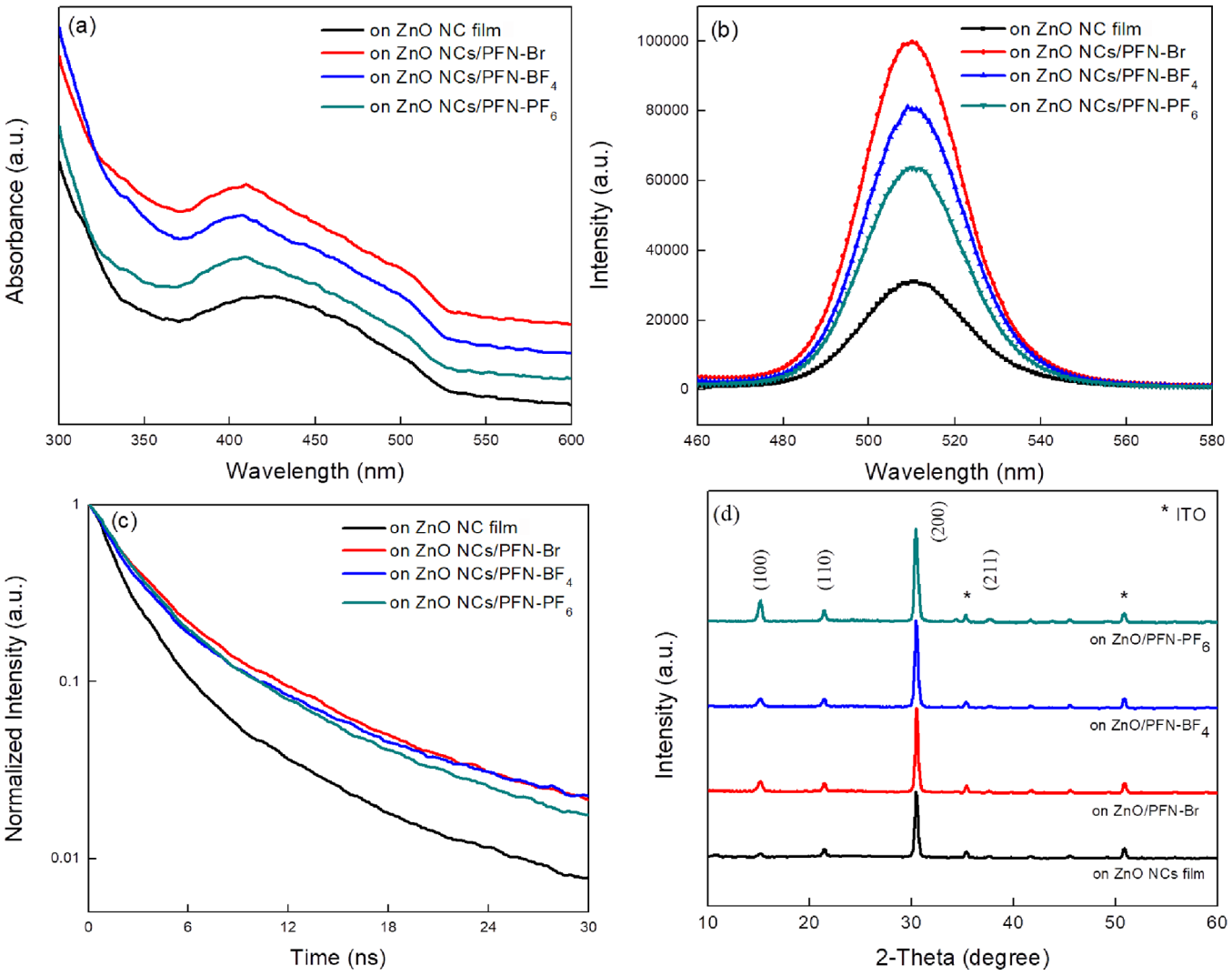

Figure 6. (a) Absorption and (b) PL spectra, (c) TR-PL decay curves, and (d) XRD patterns of $CsPbBr_3$ NCs on different ETLs. The absorption spectra are shifted vertically for clarity.

the original and CPE-modified ZnO NCs is considered to be the same. Figure 7c–f shows the luminance–voltage, current density–voltage, current efficiency–current density characteristics, and EQE plot of PeLEDs, using the original or PFN-Br-, PFN-BF_4-, PFN-PF_6-modified ZnO NC films as the ETL. A maximum luminance (L_{max}) of 811 cd/m^2 and current efficiency (η_{max}) of 0.2 cd/A were obtained for the controlled device based on the original ZnO NC film (Table 1). By depositing PFN-Br on the ZnO NC film as the ETL, the L_{max} and η_{max} of the device were significantly improved to 9321 cd/m^2 and 0.72 cd/A, respectively. By using PFN-BF_4 as the surface modifier, the elevated device performance was also received with an L_{max} of 5278 cd/m^2 and an η_{max} of 0.56 cd/A. By introducing PFN-PF_6, the corresponding PeLED showed an L_{max} of 2180 cd/m^2 and an η_{max} of 0.24 cd/A, which was still better than the controlled device. It is concluded that the luminance and current efficiency of PeLEDs are significantly enhanced by introducing CPEs between ZnO NCs and the perovskite layer. The reason behind the enhanced performance lies within the ionic groups on CPEs, which are reported to form permanent dipoles via the spontaneous orientation then facilitate the charge injection from the ETL to the active layer.[47−49] Also, the CPEs can passivate the defects on the surface of ZnO NCs and suppress nonradiative recombination to improve the brightness and current efficiency of devices. Comparing the electron injection ability of the three anionic groups Br^-, BF_4^-, and PF_6^-, it is seen that the device based on PFN-Br showed the highest brightness and current efficiency, while the other two devices based on PFN-BF_4 and PFN-PF_6 obtained lower device performance. Moreover, the device based on PFN-BF_4 exhibited better current efficiency over PFN-Br under the low current density below 160 mA/cm^2. In the early stage of this study, we expected that more effective charge injection could be achieved through fluorine-rich groups, i.e., BF_4^- and PF_6^- rather than Br^-. Therefore, we carried out the ionic exchange reaction from Br^- to BF_4^- (or PF_6^-) to obtain PFN-BF_4 (or PFN-PF_6) as the surface modifier; however, unsatisfactory device results were received. We speculate that lower device performance was obtained due to excess fluorine atoms with high electronegativity for those two groups, which tend to capture electrons instead of charge injection to the active layer. Nevertheless, the addition of fluorine-containing CPEs can still bring better performance of PeLEDs than those without CPEs. Figure 7g displays the EL spectra of devices based on different ETLs, revealing similar spectral shapes and a maximum emission wavelength at 516

https://doi.org/10.1021/acsomega.3c02593
ACS Omega 2023, 8, 19109−19118

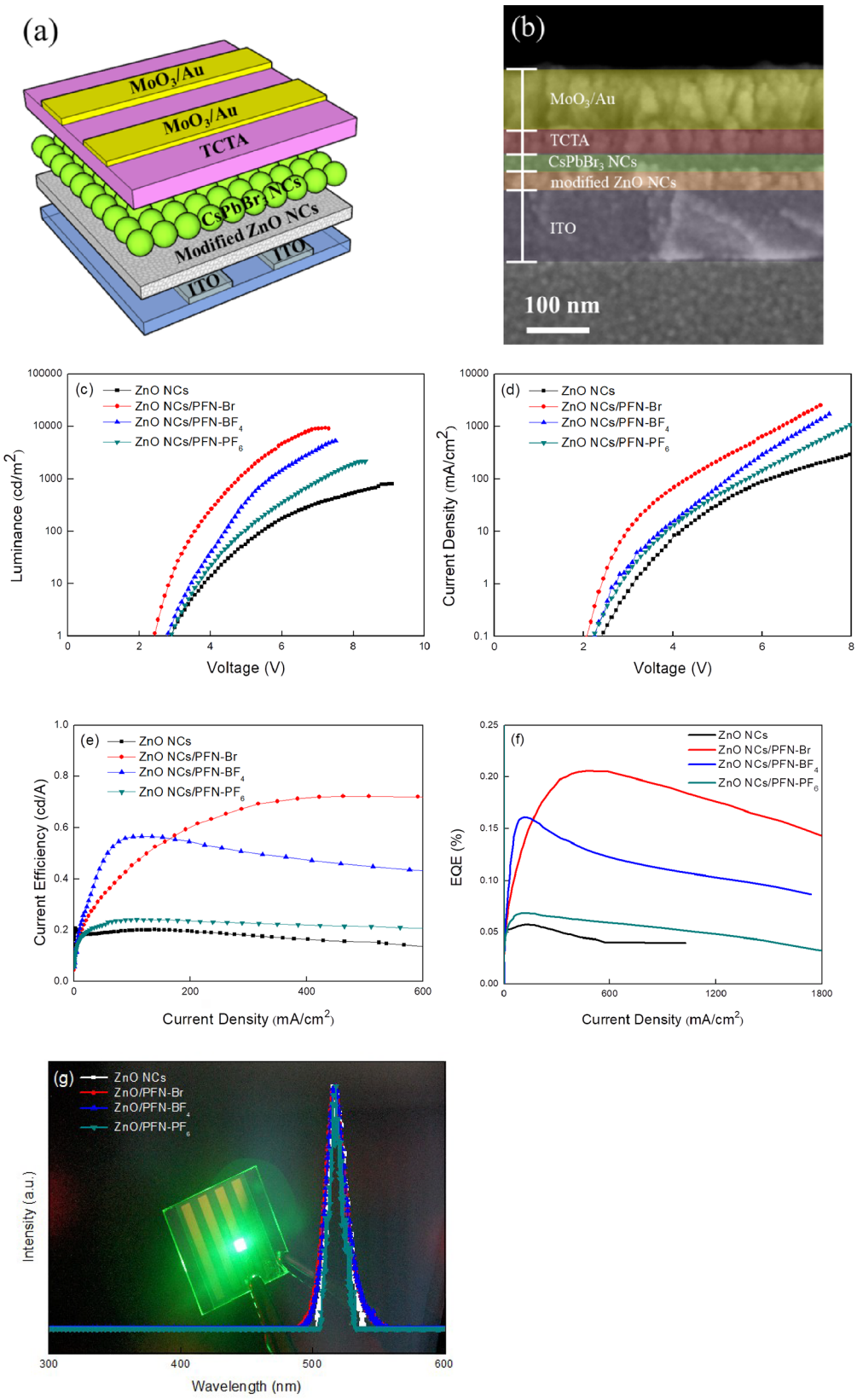

Figure 7. (a) Device structure, (b) cross-sectional SEM image, (c) brightness−voltage, (d) current density−voltage, (e) current efficiency−current density, (f) EQE, and (g) EL spectra of PeLEDs. The background in (g) shows the snapshot of the PeLED based on PFN-Br at 6 V.

nm. The wavelength difference between EL and PL spectra arises from different excitation processes. In our case, the EL maximum of the PeLED is located at 516 nm that is redshifted ~6 nm compared to the PL maximum of $CsPbBr_3$ NCs. It is reported that the slight redshift in EL spectra is originated from the photon reabsorption of the emitter or inhibition of carrier

https://doi.org/10.1021/acsomega.3c02593
ACS Omega 2023, 8, 19109−19118

Table 1. Device Performance of PeLEDs Based on the Original and CPE-Modified ZnO NC Films

ZnO type	EL (nm)	V_{on} [a] (V)	L_{max} (cd/m^2@V)	η_{max} (cd/A@V)
original	516	2.91	811@9.09	0.20@6.66
PFN-Br-modified	516	2.44	9321@7.22	0.72@5.72
PFN-BF_4-modified	516	2.81	5278@7.50	0.56@5.34
PFN-PF_6-modified	516	2.91	2180@8.25	0.24@5.72

[a]Defined as the operating voltage when the brightness reached 1 cd/m^2.

injection into smaller $CsPbBr_3$ NCs owing to larger energy barriers.[50,51] The snapshot of the strongly green emissive device using PFN-Br as the surface modifier is also included in Figure 7g. Figure 8 depicts the dark current density−voltage

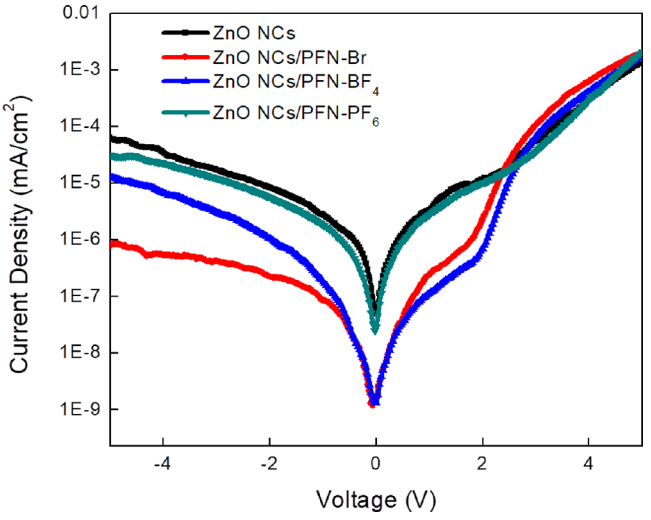

Figure 8. Dark current density−voltage characteristics of PeLEDs based on different ETLs.

curves of devices based on different ETLs under bias voltage from −5 to 5 V. The PFN-Br-modified ZnO device achieved the lowest leakage current density under negative bias, proving the best passivation ability of PFN-Br among the three CPEs that reduces surface defects of ZnO NCs and improves the device performance.[52] Meanwhile, PFN-BF_4 shows the second best passivation and electrical behavior of diodes that is accordant with the results of device performance.

CONCLUSIONS

Commercial PFN-Br was successfully converted to PFN-BF_4 or PFN-PF_6 through anion exchange for surface modification of ZnO NC films. The AFM and SEM experiments demonstrate that homogeneous and dense distribution of NCs and low surface roughness of ZnO films were obtained after introducing CPEs. The XPS results suggest a stronger interaction between the ammonium group on PFN-Br and the hydroxyl group on ZnO compared to PFN-BF_4 or PFN-PF_6. The upshifted CB of ZnO by treating with PFN-Br brings better charge injection from ZnO to $CsPbBr_3$ NCs than the other two CPEs. With the incorporation of CPEs on ZnO, it is favorable for the deposition of smooth $CsPbBr_3$ NC layers. The bandgap and emission maximum of $CsPbBr_3$ were not affected by introducing CPEs, while the PL intensity of the perovskite was strengthened because of effective surface passivation of ZnO NCs. The prolonged carrier lifetime of $CsPbBr_3$ NCs was also proven from TR-PL decay measurements. The best device performance was received from the PFN-Br-modified PeLED with an L_{max} of 9321 cd/m^2 and an η_{max} of 0.72 cd/A. Meanwhile, the device based on PFN-BF_4 exhibited the highest current efficiency among all PeLEDs under the low current density below 160 mA/cm^2. The PFN-PF_6-modified PeLED showed lower device performance than the other two CPE-modified ones due to excess fluorine atoms. Nevertheless, CPE-modified PeLEDs still exhibited higher device performance than those without CPEs, revealing the potential use of CPEs in PeLED applications.

ASSOCIATED CONTENT

Supporting Information

The Supporting Information is available free of charge at https://pubs.acs.org/doi/10.1021/acsomega.3c02593.

Carrier lifetime parameters of TR-PL decay curves of $CsPbBr_3$ NCs on different ETLs; XPS spectra of PFN-Br, PFN-BF_4, and PFN-PF_6 for Br 3d, B 1s, P 2p, and F 1s; top-view SEM images of the original, PFN-Br-, PFN-BF_4-, and PFN-PF_6-modified ZnO NC films; AFM topographic images of the original, PFN-Br-, PFN-BF_4-, and PFN-PF_6-modified ZnO NC films; XPS spectra of the O 1s element of the original and PFN-Br-, PFN-BF_4-, and PFN-PF_6-modified ZnO NC films; XPS spectra of Br 3d, B 1s, P 2p, and F 1s elements in ZnO NC films without and with CPEs; absorption spectra of ZnO NC films without and with CPEs and Tauc plot of ZnO NCs; TEM, HR-TEM micrographs, and size distribution histogram of $CsPbBr_3$ NCs; Tauc plot of $CsPbBr_3$ NCs (PDF)

AUTHOR INFORMATION

Corresponding Author

Sheng-Hsiung Yang − *Institute of Lighting and Energy Photonics, College of Photonics, National Yang Ming Chiao Tung University, Tainan 711010, Taiwan R.O.C.*; orcid.org/0000-0002-3909-3027; Email: yangsh@nycu.edu.tw

Authors

Fu-Bing Chiu − *Institute of Lighting and Energy Photonics, College of Photonics, National Yang Ming Chiao Tung University, Tainan 711010, Taiwan R.O.C.*

You-Wei Wu − *Institute of Lighting and Energy Photonics, College of Photonics, National Yang Ming Chiao Tung University, Tainan 711010, Taiwan R.O.C.*

Complete contact information is available at: https://pubs.acs.org/10.1021/acsomega.3c02593

Notes

The authors declare no competing financial interest.

ACKNOWLEDGMENTS

The authors thank the Ministry of Science and Technology, Taiwan (grant number MOST 110-2221-E-A49-082-MY3) for financially supporting this work.

REFERENCES

(1) Xiao, Z.; Kerner, R. A.; Zhao, L.; Tran, N. L.; Lee, K. M.; Koh, T.-W.; Scholes, G. D.; Rand, B. P. Efficient perovskite light-emitting

diodes featuring nanometer-sized crystallites. *Nat. Photonics* **2017**, *11*, 108−115.
(2) Zhang, K.; Zhu, N.; Zhang, M.; Wang, L.; Xing, J. Opportunities and challenges in perovskite LED commercialization. *J. Mater. Chem. C* **2021**, *9*, 3795−3799.
(3) Cho, H.; Jeong, S.-H.; Park, M.-H.; Kim, Y.-H.; Wolf, C.; Lee, C.-L.; Heo, J. H.; Sadhanala, A.; Myoung, N.; Yoo, S.; Im, S. H.; Friend, R. H.; Lee, T.-W. Overcoming the electroluminescence efficiency limitations of perovskite light-emitting diodes. *Science* **2015**, *350*, 1222−1225.
(4) Lin, K.; Xing, J.; Quan, L. N.; de Arquer, F. P. G.; Gong, X.; Lu, J.; Xie, L.; Zhao, W.; Zhang, D.; Yan, C.; Li, W.; Liu, X.; Lu, Y.; Kirman, J.; Sargent, E. H.; Xiong, Q.; Wei, Z. Perovskite light-emitting diodes with external quantum efficiency exceeding 20 per cent. *Nature* **2018**, *562*, 245−248.
(5) Veldhuis, S. A.; Boix, P. P.; Yantara, N.; Li, M.; Sum, T. C.; Mathews, N.; Mhaisalkar, S. G. Perovskite Materials for Light-Emitting Diodes and Lasers. *Adv. Mater.* **2016**, *28*, 6804−6834.
(6) Park, N.-G. Perovskite solar cells: an emerging photovoltaic technology. *Mater. Today* **2015**, *18*, 65−72.
(7) Zhang, Q.; Su, R.; Du, W.; Liu, X.; Zhao, L.; Ha, S. T.; Xiong, Q. Advances in Small Perovskite-Based Lasers. *Small Methods* **2017**, *1*, 1700163.
(8) Wang, F.; Zou, X.; Xu, M.; Wang, H.; Wang, H.; Guo, H.; Guo, J.; Wang, P.; Peng, M.; Wang, Z.; Wang, Y.; Miao, J.; Chen, F.; Wang, J.; Chen, X.; Pan, A.; Shan, C.; Liao, L.; Hu, W. Recent Progress on Electrical and Optical Manipulations of Perovskite Photodetectors. *Adv. Sci.* **2021**, *8*, 2100569.
(9) Fakharuddin, A.; Gangishetty, M. K.; Abdi-Jalebi, M.; Chin, S.-H.; bin Mohd Yusoff, A. R.; Congreve, D. N.; Tress, W.; Deschler, F.; Vasilopoulou, M.; Bolink, H. J. Perovskite light-emitting diodes. *Nat. Electron.* **2022**, *5*, 203−216.
(10) Wong, A. B.; Lai, M.; Eaton, S. W.; Yu, Y.; Lin, E.; Dou, L.; Fu, A.; Yang, P. Growth and Anion Exchange Conversion of $CH_3NH_3PbX_3$ Nanorod Arrays for Light-Emitting Diodes. *Nano Lett.* **2015**, *15*, 5519−5524.
(11) Wang, S.; Yan, S.; Wang, M.; Chang, L.; Wang, J.; Wang, Z. Construction of nanowire $CH_3NH_3PbI_3$-based solar cells with 17.62% efficiency by solvent etching technique. *Sol. Energy Mater. Sol. Cells* **2017**, *167*, 173−177.
(12) Ling, Y.; Yuan, Z.; Tian, Y.; Wang, X.; Wang, J. C.; Xin, Y.; Hanson, K.; Ma, B.; Gao, H. Bright Light-Emitting Diodes Based on Organometal Halide Perovskite Nanoplatelets. *Adv. Mater.* **2016**, *28*, 305−311.
(13) Kovalenko, M. V.; Protesescu, L.; Bodnarchuk, M. I. Properties and potential optoelectronic applications of lead halide perovskite nanocrystals. *Science* **2017**, *358*, 745−750.
(14) Protesescu, L.; Yakunin, S.; Bodnarchuk, M. I.; Krieg, F.; Caputo, R.; Hendon, C. H.; Yang, R. X.; Walsh, A.; Kovalenko, M. V. Nanocrystals of Cesium Lead Halide Perovskites ($CsPbX_3$, X = Cl, Br, and I): Novel Optoelectronic Materials Showing Bright Emission with Wide Color Gamut. *Nano Lett.* **2015**, *15*, 3692−3696.
(15) Parobek, D.; Dong, Y.; Qiao, T.; Son, D. H. Direct Hot-Injection Synthesis of Mn-Doped $CsPbBr_3$ Nanocrystals. *Chem. Mater.* **2018**, *30*, 2939−2944.
(16) Wang, C.; Zhang, C.; Wang, F.; Chen, J.; Ren, E.; Kong, J.; Li, L.; Xu, J.; Zhang, Y. Synthesis of highly luminescent $CsPbBr_3$@Cs_4PbBr_6 nanocrystals via ligand-assisted reaction. *Opt. Mater.* **2022**, *128*, No. 112444.
(17) Li, Y.; Huang, H.; Xiong, Y.; Kershaw, S. V.; Rogach, A. L. Revealing the Formation Mechanism of $CsPbBr_3$ Perovskite Nanocrystals Produced via a Slowed-Down Microwave-Assisted Synthesis. *Angew. Chem., Int. Ed.* **2018**, *57*, 5833−5837.
(18) Rao, L.; Tang, Y.; Song, C.; Xu, K.; Vickers, E. T.; Bonabi Naghadeh, S.; Ding, X.; Li, Z.; Zhang, J. Z. Polar-Solvent-Free Synthesis of Highly Photoluminescent and Stable $CsPbBr_3$ Nanocrystals with Controlled Shape and Size by Ultrasonication. *Chem. Mater.* **2019**, *31*, 365−375.
(19) Chen, D.; Fang, G.; Chen, X.; Lei, L.; Zhong, J.; Mao, Q.; Zhou, S.; Li, J. Mn-Doped $CsPbCl_3$ perovskite nanocrystals: solvothermal synthesis, dual-color luminescence and improved stability. *J. Mater. Chem. C* **2018**, *6*, 8990−8998.
(20) Pan, J.; Quan, L. N.; Zhao, Y.; Peng, W.; Murali, B.; Sarmah, S. P.; Yuan, M.; Sinatra, L.; Alyami, N. M.; Liu, J.; Yassitepe, E.; Yang, Z.; Voznyy, O.; Comin, R.; Hedhili, M. N.; Mohammed, O. F.; Lu, Z. H.; Kim, D. H.; Sargent, E. H.; Bakr, O. M. Highly Efficient Perovskite-Quantum-Dot Light-Emitting Diodes by Surface Engineering. *Adv. Mater.* **2016**, *28*, 8718−8725.
(21) He, S.; Kumar, N.; Lee, H. B.; Ko, K.-J.; Jung, Y.-J.; Kim, J. I.; Bae, S.; Lee, J.-H.; Kang, J.-W. Tailoring the refractive index and surface defects of $CsPbBr_3$ quantum dots via alkyl cation-engineering for efficient perovskite light-emitting diodes. *Chem. Eng. J.* **2021**, *425*, No. 130678.
(22) Kim, Y.-H.; Han, T.-H.; Cho, H.; Min, S.-Y.; Lee, C.-L.; Lee, T.-W. Polyethylene Imine as an Ideal Interlayer for Highly Efficient Inverted Polymer Light-Emitting Diodes. *Adv. Funct. Mater.* **2014**, *24*, 3808−3814.
(23) Bolink, H. J.; Coronado, E.; Sessolo, M. White Hybrid Organic-Inorganic Light-Emitting Diode Using ZnO as the Air-Stable Cathode. *Chem. Mater.* **2009**, *21*, 439−441.
(24) Navas, D.; Fuentes, S.; Castro-Alvarez, A.; Chavez-Angel, E. Review on Sol-Gel Synthesis of Perovskite and Oxide Nanomaterials. *Gels* **2021**, *7*, 275.
(25) Kołodziejczak-Radzimska, A.; Jesionowski, T. Zinc Oxide—From Synthesis to Application: A Review. *Materials* **2014**, *7*, 2833−2881.
(26) Shan, Q.; Song, J.; Zou, Y.; Li, J.; Xu, L.; Xue, J.; Dong, Y.; Han, B.; Chen, J.; Zeng, H. High Performance Metal Halide Perovskite Light-Emitting Diode: From Material Design to Device Optimization. *Small* **2017**, *13*, 1701770.
(27) Tang, C.; Shen, X.; Wu, X.; Zhong, Y.; Hu, J.; Lu, M.; Wu, Z.; Zhang, Y.; Yu, W. W.; Bai, X. Optimizing the Performance of Perovskite Nanocrystal LEDs Utilizing Cobalt Doping on a ZnO Electron Transport Layer. *J. Phys. Chem. Lett.* **2021**, *12*, 10112−10119.
(28) Kumar, G. S.; Pradhan, B.; Kamilya, T.; Acharya, S. Enhancing Performances of Hybrid Perovskite Light Emitting Diodes with Thickness Controlled PMMA Interlayer. *Bull. Chem. Soc. Jpn.* **2018**, *91*, 1241−1248.
(29) Wang, J.; Wang, N.; Jin, Y.; Si, J.; Tan, Z.-K.; Du, H.; Cheng, L.; Dai, X.; Bai, S.; He, H.; Ye, Z.; Lai, M. L.; Friend, R. H.; Huang, W. Interfacial Control Toward Efficient and Low-Voltage Perovskite Light-Emitting Diodes. *Adv. Mater.* **2015**, *27*, 2311−2316.
(30) Chen, L.; Lee, M.-H.; Wang, Y.; Lau, Y. S.; Syed, A. A.; Zhu, F. Interface dipole for remarkable efficiency enhancement in all-solution-processable transparent inverted quantum dot light-emitting diodes. *J. Mater. Chem. C* **2018**, *6*, 2596−2603.
(31) Shin, Y. S.; Yoon, Y. J.; Heo, J.; Song, S.; Kim, J. W.; Park, S. Y.; Cho, H. W.; Kim, G.-H.; Kim, J. Y. Functionalized PFN-X (X = Cl, Br, or I) for Balanced Charge Carriers of Highly Efficient Blue Light-Emitting Diodes. *ACS Appl. Mater. Interfaces* **2020**, *12*, 35740−35747.
(32) Chiu, P.-C.; Yang, S.-H. Improvement in hole transporting ability and device performance of quantum dot light emitting diodes. *Nanoscale Adv.* **2020**, *2*, 401−407.
(33) Zhao, C.; Liang, Y.; Li, W.; Chen, X.; Tian, Y.; Yin, D.; Zhang, Q. 3D BiOBr/BiOCl heterostructure microspheres with enhanced photocatalytic activity. *J. Mater. Sci.: Mater. Electron.* **2020**, *31*, 1868−1878.
(34) Gupta, A. K.; Singh, R. K.; Chandra, S. Crystallization kinetics behavior of ionic liquid [EMIM][BF_4] confined in mesoporous silica matrices. *RSC Adv.* **2014**, *4*, 22277−22287.
(35) Oikonomou, C.; Hryha, E.; Nyborg, L. An XPS investigation on the thermal stability of the insulating surface layer of soft magnetic composite powder. *Surf. Interface Anal.* **2016**, *48*, 445−450.
(36) Seo, S. Y.; Park, J.; Kang, Y.-C. Chemical Analysis of Ionic Liquids Using Photoelectron Spectroscopy. *Bull. Korean Chem. Soc.* **2016**, *37*, 355−360.

https://doi.org/10.1021/acsomega.3c02593
ACS Omega 2023, 8, 19109−19118

(37) Garino, N.; Limongi, T.; Dumontel, B.; Canta, M.; Racca, L.; Laurenti, M.; Castellino, M.; Casu, A.; Falqui, A.; Cauda, V. A Microwave-Assisted Synthesis of Zinc Oxide Nanocrystals Finely Tuned for Biological Applications. *Nanomaterials* **2019**, *9*, 212.
(38) Park, M.; Roh, J.; Lim, J.; Lee, H.; Lee, D. Double Metal Oxide Electron Transport Layers for Colloidal Quantum Dot Light-Emitting Diodes. *Nanomaterials* **2020**, *10*, 726.
(39) Sun, Y.; Jiang, Y.; Peng, H.; Wei, J.; Zhang, S.; Chen, S. Efficient quantum dot light-emitting diodes with a $Zn_{0.85}Mg_{0.15}O$ interfacial modification layer. *Nanoscale* **2017**, *9*, 8962−8969.
(40) Kuan, C.-H.; Yang, S.-H. Surface ligand engineering of perovskite nanocrystals with a conjugated sulfonate ligand for light-emitting applications. *Mater. Adv.* **2022**, *3*, 7824−7832.
(41) Choi, H.; Park, J. S.; Jeong, E.; Kim, G.-H.; Lee, B. R.; Kim, S. O.; Song, M. H.; Woo, H. Y.; Kim, J. Y. Combination of Titanium Oxide and a Conjugated Polyelectrolyte for High-Performance Inverted-Type Organic Optoelectronic Devices. *Adv. Mater.* **2011**, *23*, 2759−2763.
(42) Shen, K.; Li, X.; Xu, H.; Wang, M.; Dai, X.; Guo, J.; Zhang, T.; Li, S.; Zou, G.; Choy, K.-L.; Parkin, I. P.; Guo, Z.; Liu, H.; Wu, J. Enhanced performance of ZnO nanoparticle decorated all-inorganic $CsPbBr_3$ quantum dot photodetectors. *J. Mater. Chem. A* **2019**, *7*, 6134−6142.
(43) Ji, W.; Liu, S.; Zhang, H.; Wang, R.; Xie, W.; Zhang, H. Ultrasonic Spray Processed, Highly Efficient All-Inorganic Quantum-Dot Light-Emitting Diodes. *ACS Photonics* **2017**, *4*, 1271−1278.
(44) Guo, M.-L.; Lu, Y.; Cai, X.-Y.; Shen, Y.; Qian, X.-Y.; Ren, H.; Li, Y.-Q.; Wang, W.-J.; Tang, J.-X. Interface engineering improves the performance of green perovskite light-emitting diodes. *J. Mater. Chem. C* **2022**, *10*, 2998−3005.
(45) Chen, C.; Xuan, T.; Bai, W.; Zhou, T.; Huang, F.; Xie, A.; Wang, L.; Xie, R.-J. Highly stable $CsPbI_3$:Sr^{2+} nanocrystals with near-unity quantum yield enabling perovskite light-emitting diodes with an external quantum efficiency of 17.1%. *Nano Energy* **2021**, *85*, No. 106033.
(46) Zheng, C.; Bi, C.; Huang, F.; Binks, D.; Tian, J. Stable and Strong Emission $CsPbBr_3$ Quantum Dots by Surface Engineering for High-Performance Optoelectronic Films. *ACS Appl. Mater. Interfaces* **2019**, *11*, 25410−25416.
(47) Zhu, X.; Xie, Y.; Li, X.; Qiao, X.; Wang, L.; Tu, G. Anionic conjugated polyelectrolyte−wetting properties with an emission layer and free ion migration when serving as a cathode interface layer in polymer light emitting diodes (PLEDs) *J. Mater. Chem.* **2012**, *22*, 15490−15494.
(48) Liu, H.; Hu, L.; Wu, F.; Chen, L.; Chen, Y. Polyfluorene Electrolytes Interfacial Layer for Efficient Polymer Solar Cells: Controllably Interfacial Dipoles by Regulation of Polar Groups. *ACS Appl. Mater. Interfaces* **2016**, *8*, 9821−9828.
(49) Lee, W.; Seo, J. H.; Woo, H. Y. Conjugated polyelectrolytes: A new class of semiconducting material for organic electronic devices. *Polymer* **2013**, *54*, 5104−5121.
(50) Wu, W.; Zhang, Y.; Liang, T.; Fan, J. Carrier accumulation enhanced Auger recombination and inner self-heating-induced spectrum fluctuation in $CsPbBr_3$ perovskite nanocrystal light-emitting devices. *Appl. Phys. Lett.* **2019**, *115*, 243503.
(51) Zhang, W.; Dai, D.; Chen, X.; Guo, X.; Fan, J. Red shift in the photoluminescence of colloidal carbon quantum dots induced by photon reabsorption. *Appl. Phys. Lett.* **2014**, *104*, No. 091902.
(52) Gangishetty, M. K.; Hou, S.; Quan, Q.; Congreve, D. N. Reducing Architecture Limitations for Efficient Blue Perovskite Light-Emitting Diodes. *Adv. Mater.* **2018**, *30*, 1706226.

https://doi.org/10.1021/acsomega.3c02593
ACS Omega 2023, 8, 19109−19118